



Cite this: DOI: 10.1039/c7ta10678e

# High performance low-temperature solid oxide fuel cells with atomic layer deposited-yttria stabilized zirconia embedded thin film electrolyte†

Seongkook Oh,<sup>a</sup> Joonsuk Park,<sup>b</sup> Jeong Woo Shin,<sup>a</sup> Byung Chan Yang,<sup>a</sup> Jiaming Zhang,<sup>c</sup> Dong Young Jang<sup>a</sup> and Jihwan An<sup>id</sup> \*<sup>a</sup>

We report the design and the fabrication of a sandwich-structured thin-film composite electrolyte for low-temperature solid oxide fuel cells supported by a nanoporous anodized aluminum oxide (AAO) substrate. We adopt an extremely thin (25 nm) atomic-layer-deposited (ALD) yttria-stabilized zirconia (YSZ) layer embedded in highly ionic-conductive sputtered samaria-doped ceria (SDC) electrolytes (360 nm thick) and systematically vary the position of the YSZ layer to investigate the optimal design of the composite electrolyte. The cell with a sputtered SDC (180 nm)/ALD YSZ (25 nm)/sputtered SDC (180 nm) sandwich electrolyte shows a high maximum power density of 562 mW cm<sup>-2</sup> at 450 °C, which is the highest performance at this temperature range for AAO-supported cells to date.

Received 5th December 2017  
Accepted 5th February 2018

DOI: 10.1039/c7ta10678e

rsc.li/materials-a

## Introduction

Solid oxide fuel cells (SOFCs) have drawn considerable attention because of their advantages for use as next-generation energy conversion devices, including high efficiency, environmental friendliness, and fuel flexibility. Conventional SOFCs are usually operated at high temperatures ranging from 800 to 1000 °C, which poses practical problems regarding thermal degradation and material selection.<sup>1–4</sup> Research on SOFCs driven in the mid-temperature range (600–800 °C) or the low-temperature range (<500 °C), therefore, has recently been conducted.<sup>3,5–18</sup> However, in the low-temperature region, the ionic conductivity of the electrolyte drops and the ohmic loss increases greatly.<sup>3,19,20</sup> The electrochemical reaction at the electrode–electrolyte interface also becomes slow, especially on the cathode side, owing to the sluggish oxygen reduction reaction; therefore, the activation loss is also increased.

To reduce the ohmic resistance at low temperature, one can fabricate an SOFC with a thin-film electrolyte (thickness <1 μm), that is, a thin-film SOFC (TF-SOFC).<sup>8–18</sup> TF-SOFCs, however, are known to lack the mechanical strength necessary for stable operation, so supporting structures are usually necessary. TF-SOFCs can be categorized into two types depending on the

supporting structure: Si-based free-standing and porous-substrate-supported cells. The use of free-standing cells is beneficial for maximizing the power density; for example, a Si-based free-standing TF-SOFC with a high power density of 1.3 W cm<sup>-2</sup> at 450 °C has been reported.<sup>9</sup> However, the functioning area of Si-based free-standing cells is generally limited by the mechanical stability of the membrane during fabrication and operation despite recent progress in the cell architecture to improve the mechanical stability.<sup>12</sup> The cell fabrication also requires relatively expensive microfabrication processes such as dry-etching and photolithography.<sup>8–12</sup> In contrast, TF-SOFCs supported by nanoporous substrates, *e.g.*, anodized aluminum oxide (AAO), Ni-doped zirconia/doped ceria, Ni foam, and porous stainless steel, can provide both scalability and mechanical stability without the need for etching or photolithography processes.<sup>13–18</sup> However, the relatively low power density of these cells compared to that of free-standing ones, *i.e.*, the best performance of AAO-supported thin film LT-SOFCs ever reported is 380 mW cm<sup>-2</sup> at 450 °C,<sup>18</sup> indicates a need to optimize the design of the thin-film membrane–electrode assembly for smaller losses and thus higher performance.

The optimal design of the electrolyte for a TF-SOFC should meet the following requirements to minimize the losses.<sup>21</sup> First, thin films with high ionic conductivity should be used to minimize the ohmic loss. In addition, the surface of the electrolyte should support a high surface exchange reaction, especially at the cathode; therefore, materials with high surface exchange are preferred. Finally, the electrolyte should not be electrically conductive even at the operating temperature for a high open-circuit voltage (OCV).

In this regard, doped CeO<sub>2</sub> is a promising electrolyte material with high ionic conductivity as well as a high surface exchange

<sup>a</sup>Department of Manufacturing Systems and Design Engineering (MSDE), Seoul National University of Science and Technology, 232 Gongneung-ro, Nowon-gu, Seoul 01811, Republic of Korea. E-mail: jihwanan@seoultech.ac.kr; Fax: +82-2-974-5388; Tel: +82-2-970-7276

<sup>b</sup>Department of Materials Science and Engineering, Stanford University, Stanford, CA 94305, USA

<sup>c</sup>Hewlett Packard Labs, 1501 Page Mill Rd, Palo Alto, CA 94304, USA

† Electronic supplementary information (ESI) available. See DOI: 10.1039/c7ta10678e

coefficient; in particular, the ionic conductivity of samaria-doped ceria (SDC) is superior, *i.e.*, 2 orders higher than that of yttria-stabilized zirconia (YSZ) at near 500 °C, and SDC also shows high surface exchange owing to the large size of the dopant ions ( $\text{Sm}^{3+}$ , 109.8 pm) compared to other dopant ions ( $\text{Gd}^{3+}$ , 107.8 pm;  $\text{Y}^{3+}$ , 104 pm).<sup>22,23</sup> However, due to its chemical instability, doped ceria such as SDC exhibits electrical conductivity even at relatively low temperatures of less than 500 °C, resulting in low OCV values if it is used alone; indeed, Ji *et al.* reported that a TF-SOFC with an 850 nm-thick gadolinia-doped ceria (GDC) electrolyte showed a low OCV of 0.3 V at 450 °C.<sup>13</sup> The reduction in the OCV can be effectively prevented by adopting a pinhole-free blocking layer that is chemically stable at elevated temperature, such as YSZ;<sup>13</sup> however, the ohmic resistance may significantly increase if the thickness of the blocking layer is not minimized. Furthermore, YSZ may impede the facile charge transfer reaction if it is used at the outermost surface of the electrolyte owing to its lower surface exchange coefficient compared to other doped ceria materials.<sup>20</sup> A pinhole-free and conformal YSZ layer can be fabricated by atomic layer deposition (ALD), a variant of chemical vapor deposition, which is known to provide pinhole-free, dense, and conformal thin films.<sup>8–16,18</sup> However, the thickness and location of the atomic-layer-deposited YSZ layer in previous publications have not been optimized for the application to a TF-SOFC electrolyte, resulting in relatively low performance. While the thickness of the YSZ layer needed for complete electron blocking is much thinner when fabricated with ALD compared to physical vapor deposition techniques (*e.g.*, pulsed laser deposition (PLD)), still relatively thick (total thickness >100 nm) ALD YSZ layers have been used as sole electrolytes or at the anode/cathode side surfaces of electrolytes of AAO-based TF-SOFCs, which has led to relatively large ohmic and activation resistances.<sup>13,14,16,18,24</sup>

In this paper, we report the design and the fabrication of a sandwich-structured sputtered SDC/ALD YSZ composite electrolyte for a high-performance AAO-supported TF-SOFC by a combination of optimal processes and materials. While the sandwich-structured electrolyte design has been previously reported,<sup>26,27</sup> *e.g.*, PLD GDC/YSZ/GDC structure, our electrolyte design has significantly helped to improve the cell performance due to the following advantages: (1) a high OCV is obtained by using a chemically stable conformal YSZ layer fabricated by ALD, (2) high surface exchange at the electrode–electrolyte interfaces is obtained by adopting SDC layers with nanogranular surfaces, and (3) low ohmic resistance is obtained by using highly ion conductive SDC and ultrathin YSZ layers. Through a systematic investigation of the optimal position of the ALD YSZ layer in the SDC–YSZ composite electrolyte, we report that the cell with the optimally designed electrolyte, *i.e.*, ALD YSZ embedded in sputtered SDC, yields the highest maximum power density of 562 mW cm<sup>-2</sup> for AAO-supported cells at 450 °C.

## Experiments

### Cell fabrication

To make AAO-based TF-SOFCs, commercially available AAO substrates were used as supports (InRedox, 1 cm × 1 cm and

100 μm in thickness, with a 55 nm-diameter pore size) (Fig. S1(a)†). A 300 nm-thick Pt anode was deposited by DC magnetron sputtering under an Ar atmosphere with a pressure of 5 mTorr and a DC power of 400 W. The surface of the Pt anode shows a porous structure stemming from the underlying AAO substrate's pores (Fig. S1(b)†). SDC and YSZ were used as electrolyte materials. The SDC electrolyte was deposited by RF sputtering under a mixed Ar and O<sub>2</sub> atmosphere (4 : 1) at a pressure of 5 mTorr and a RF power of 200 W (SRN-110, Sorona). The growth rate of the SDC film was 1.5 nm min<sup>-1</sup>. Atomic layer deposition (ALD) was used to deposit the thin-film YSZ layer. Tris(methylcyclopentadienyl)yttrium ((CpCH<sub>3</sub>)<sub>3</sub>Y) and tetrakis(methylethylamino) zirconium (TEMA Zr) were used as precursors for Y<sub>2</sub>O<sub>3</sub> and ZrO<sub>2</sub>, respectively. The Zr and Y precursors were maintained at 190 °C and 75 °C, respectively, and the deposition temperature was maintained at 225 °C. H<sub>2</sub>O and N<sub>2</sub> gases were used as the oxygen source and the carrier gas, respectively. Both the ZrO<sub>2</sub> and Y<sub>2</sub>O<sub>3</sub> processes show a growth rate per cycle (GPC) of ~1.0 Å per cycle. To dope ZrO<sub>2</sub> with Y<sub>2</sub>O<sub>3</sub>, the ZrO<sub>2</sub>–Y<sub>2</sub>O<sub>3</sub> composite film was deposited with a cycle ratio of 5 : 1 (ZrO<sub>2</sub> : Y<sub>2</sub>O<sub>3</sub>). The growth rate per supercycle (5 ZrO<sub>2</sub> cycles + 1 Y<sub>2</sub>O<sub>3</sub> cycle) was ~6 Å per supercycle.

Four samples were prepared with different combinations of ALD YSZ and sputtered SDC layers. ALD YSZ layers (25 nm thick) were located at the anode-side surface, at the cathode-side surface, and in the middle of the 360 nm-thick SDC electrolyte (namely, the CZ, CZC, and ZC samples, respectively) (Fig. 1). The sample without an ALD YSZ layer (360 nm-thick SDC only) was set as the reference. An 80 nm-thick porous Pt cathode was deposited

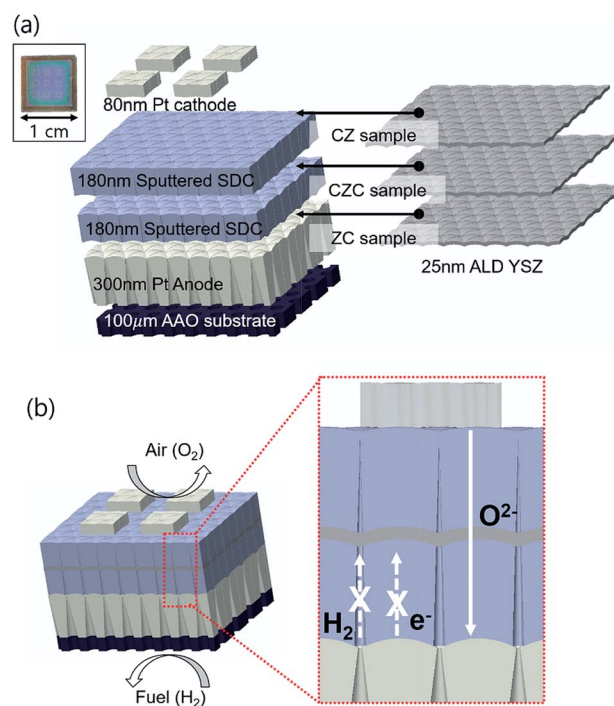


Fig. 1 Schematics of (a) sample structures of CZ, CZC, and ZC samples (the photo of the actual cell is in the inset image) and (b) operation principle of the CZC sample.

by DC sputtering in an Ar atmosphere with a pressure of 40 mTorr and a sputtering power of 300 W on the electrolyte surface of all four samples (Fig. S1(c)†). A physical mask with a 1 mm × 1 mm window was used to define the area of the cathode.

### Electrochemical analysis

Electrochemical performances of the SOFC samples were analyzed in a customized test station built on a temperature-controllable heater (Fig. S2†). Dry hydrogen gas (20 sccm) was supplied to the anode through the pores of the AAO template, and the cathode was exposed to ambient air. Electrochemical

analysis such as OCV characterization, linear sweep voltammetry (LSV) (for current–voltage measurement), and electrochemical impedance spectroscopy (EIS) were performed at 450 °C using a potentiostat (Sp-200, Bio-logic). LSV analysis started 5 s after OCV measurement at a scan rate of 20 mV s<sup>-1</sup> from the OCV to 0.1 V. EIS analysis was conducted at cell voltages of 0.8 V and 0.6 V in the frequency range of 100 kHz to 1 Hz with a sinusoidal AC voltage perturbation of 50 mV in amplitude.

### Chemical and morphological analysis

X-ray photoelectron spectroscopy (XPS) was used for compositional analysis (K-Alpha+, ThermoFisher Scientific) with an Al K $\alpha$  source gun, a spot size of 400 nm<sup>2</sup>, a step size of 1 eV per step, and a binding energy range of 0–1000 eV. The surface morphology of the composite electrode was investigated using a field emission scanning electron microscope (FE-SEM, SU8010, Hitachi). To observe the cross-sectional morphology and composition, a transmission electron microscope (TEM, FEI Tecnai G2 F20 X-TWIN), a scanning transmission electron microscope (STEM, HP Lab, FEI double-corrected Titan), and energy-dispersive spectrometer (EDS, Super EDS, 20 kV dispersion, Bruker) were used. Samples for TEM/STEM characterization were prepared by using a focused ion beam (FIB, FET Strata 235DB dual-beam FIB/SEM) lift-out technique. The TEM was operated in a bright field mode at an acceleration voltage of 80 kV. The STEM was operated in a dark field mode at an acceleration voltage of 200 kV, a spot size of 7 nm, and a screen current of ~500 pA. Atomic force microscopy (AFM, SPM-1000, AIST-NT) was also used for surface morphology characterization.

## Results and discussion

From the X-ray photoelectron spectroscopy (XPS) measurement, the doping ratios of sputtered SDC (Sm 10.5 at%, Ce 29.2 at%, and O 59.9 at%) and ALD YSZ (Y 6.3 at%, Zr 26.8 at%, and O 65.0 at%) were confirmed to be 15.2 mol% and 10.5 mol%, respectively, with negligible impurity content ( $C < 2$  at%) (Fig. 2). TEM

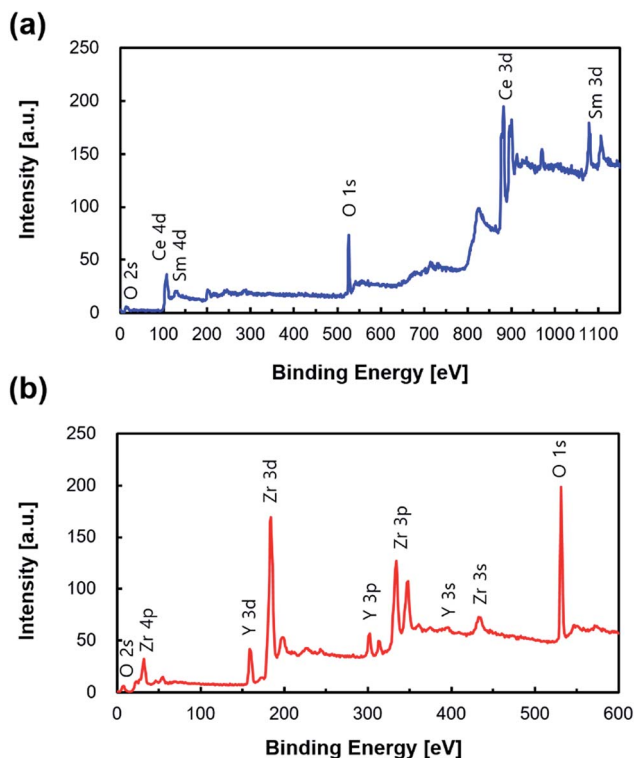


Fig. 2 XPS spectra of (a) SDC and (b) YSZ films.

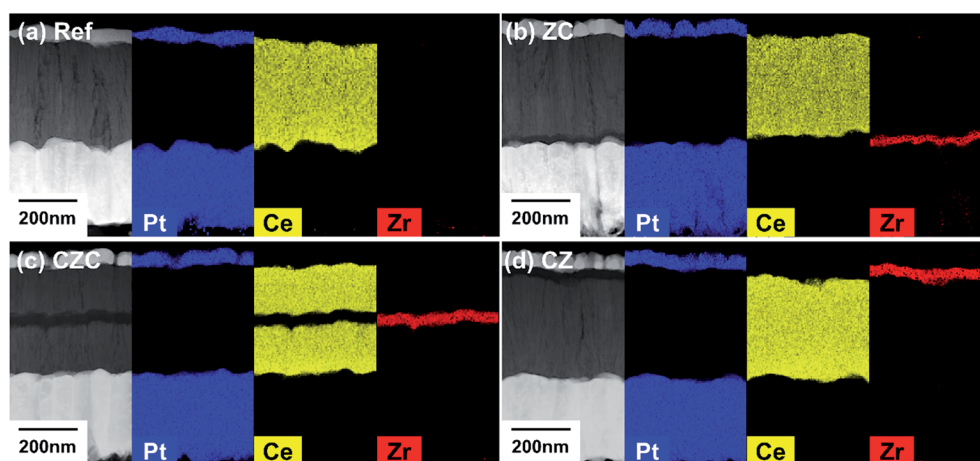


Fig. 3 Cross-sectional TEM images and EDS mapping of Ce, Zr, and Pt: (a) reference sample, (b) ZC sample, (c) CZC sample and (d) CZ sample.

imaging and EDS mapping techniques were used to analyze the cross-sectional structure and the composition of the reference, ZC, CZC, and CZ samples (Fig. 3). The total thickness of the SDC layer was 360 nm in all the samples. The sputtered SDC layers of all the samples showed columnar grain structures with vertically aligned grain boundaries (dark region inside the SDC layer). In the ZC, CZC, and CZ samples, the ALD YSZ layers were inserted on the anode side, in the middle, and on the cathode side of the electrolyte, respectively. The ALD YSZ layers are dense and cover the underlying structures conformally in all the samples owing to the nature of the atomic layer deposition process, as was previously mentioned.<sup>8–14</sup> The thickness of the ALD YSZ layer in the ZC sample, however, is slightly thinner than those in CZC and CZ samples ( $20.9 \pm 0.2$  nm (ZC sample),  $26.8 \pm 0.3$  nm (CZC sample), and  $26.4 \pm 0.5$  nm (CZ sample)); this could be because the oxide formation on the Pt surface is thermodynamically unfavorable, which leads to the delay of ALD film nucleation due to the absence of hydroxyl groups.<sup>28</sup> The Pt top cathode and bottom anode have thicknesses of 80 nm and 300 nm, respectively, and exhibit porous structures with columnar grains, which are beneficial for facilitating electrochemical reactions (see also Fig. S1(b) and S1(c)†).

Fig. 4(a) shows the OCV values of the four samples. The reference sample without an ALD YSZ layer recorded a low OCV of 0.37 V. This low OCV may be the result of a partial chemical short caused by pinholes in the sputtered SDC layer (Fig. 4(a)) or an electrical short between the anode and the cathode due to reduction of the SDC electrolyte at the operating temperature ( $450^\circ\text{C}$ ).<sup>17,21</sup> On the other hand, the CZ, CZC, and ZC samples with ALD YSZ layers showed high OCVs of 1.05 V, 1.04 V, and 1.04 V, respectively, which are close to the OCVs of other  $\text{H}_2(\text{dry})\text{-O}_2$  TF-SOFCs reported elsewhere (1.05–1.1 V).<sup>16,18,24–26</sup> The CZC sample also maintained its OCV for an extended operating time of over 15 h (Fig. 4(b)) because the possible shorting is prevented by the pinhole-free nature and chemical stability of the ALD YSZ film. To function as an effective blocking layer for electrical and chemical shorts, the ALD YSZ layer has to satisfy two requirements:<sup>13,29,30</sup> (1) the YSZ-to-SDC thickness ratio should meet the minimum limit to prevent electrical conduction, and (2) the ALD YSZ layer should form a complete (*i.e.*, pinhole-free) conformal film to block chemical conduction. Kwon *et al.* reported that the thickness ratio of the YSZ layer to the doped ceria layer should be  $\geq 10^{-4}$  at  $800^\circ\text{C}$  to prevent reduction of the ceria, and the minimum ratio decreases as the temperature decreases. Therefore, the required minimum thickness of the YSZ layer for electron blockage at  $450^\circ\text{C}$ , if the thickness of the SDC layer is 360 nm, is only  $<0.1$  nm.<sup>13,29</sup> A thicker film, however, is usually needed for conformal coverage of substrates; on rough substrates such as a Pt anode on an AAO substrate (Fig. S1(b)†), for example, even a 35 nm-thick YSZ thin film deposited by plasma-enhanced atomic layer deposition was not sufficient to completely cover the substrates, which led to a relatively low OCV ( $\sim 0.8$  V) because of uneven coverage of the YSZ layer on the Pt anode.<sup>14</sup> The better conformability of the thermal ALD YSZ film compared to the plasma-enhanced ALD film, as shown in many reports previously, seems to have improved the blocking effect

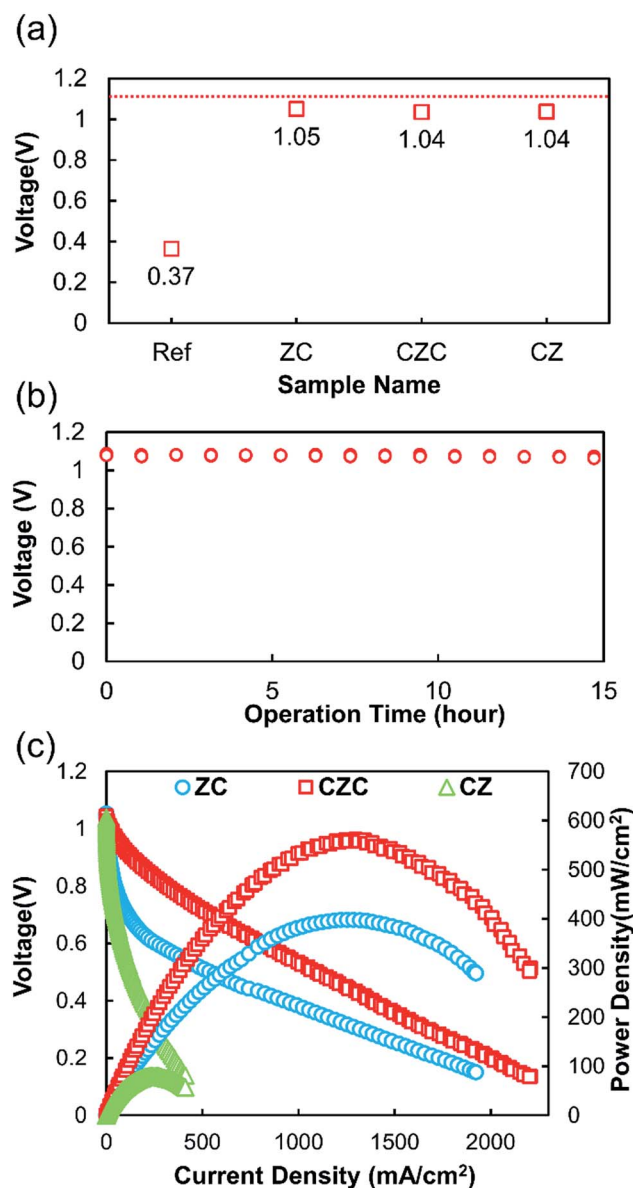


Fig. 4 Electrochemical characterization results of the reference, CZ, ZC, and CZC samples: (a) OCV values (red line is theoretical OCV, *i.e.*, 1.1 V at  $450^\circ\text{C}$ ), (b) OCV of the CZC sample for 15 h, and (c) polarization curves of CZ, ZC, and CZC samples.

in our samples. Fig. 4(c) shows the polarization curves of the ZC, CZC, and CZ samples at  $450^\circ\text{C}$ , which showed maximum power densities of 398, 562, and  $80\text{ mW cm}^{-2}$ , respectively. The highest performance was achieved when the extremely thin ALD YSZ layer was located in the middle of the SDC-based electrolyte. Compared to the best performance of AAO-supported TF-SOFCs ever reported ( $380\text{ mW cm}^{-2}$  at  $450^\circ\text{C}$  by Hong *et al.*),<sup>18</sup> our SOFC (CZC sample) shows  $\sim 50\%$  higher maximum power density at the same operating temperature.

EIS was performed to investigate the effect of the individual resistances on the overall performance of the fuel cell (Fig. 5). Fig. 5(a)–(c) show the Nyquist plots at 0.8 V and 0.6 V of the ZC, CZC, and CZ samples, respectively. All the spectra start from  $0.22 \pm 0.02\ \Omega\ \text{cm}^2$  at high frequency (100 kHz), regardless of the

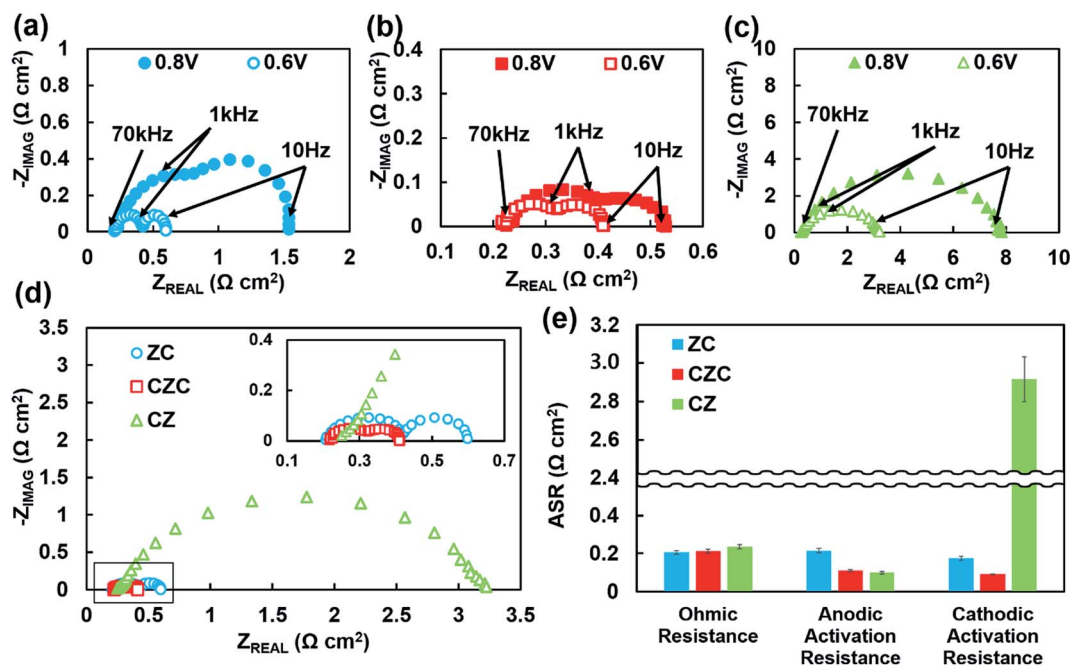


Fig. 5 EIS results of the ZC, CZC, and CZ samples: EIS spectra at 0.8 V (filled) and 0.6 V (hollow) of (a) ZC, (b) CZC, and (c) CZ samples. (d) EIS spectra of the samples in one plot at 0.6 V. (e) Summary of area-specific resistances (ASRs) for ohmic, anodic activation, and cathodic activation resistances.

bias voltage, and two semicircles whose magnitudes change with the bias voltage are observed. Therefore, the resistance of  $0.22 \pm 0.02 \Omega \text{ cm}^2$  can be regarded as the ohmic resistance.<sup>21</sup> The two semicircles in the lower-frequency region seem to correspond to the activation resistances stemming from the anode (100–1 kHz) and cathode (<1 kHz).<sup>21</sup> While various electrode reactions such as the surface reaction or charge transfer could contribute to the size of each of these semicircles, it is generally accepted that the corresponding frequency of the overall anode reaction is much larger than that of overall cathode reactions ( $\sim 2$  orders of magnitude).<sup>31</sup> In the previous literature on AAO-based TF-SOFCs, a clear distinction between anode and cathode semicircles was also reported in similar frequency ranges.<sup>16,17</sup> As shown in the  $I$ - $V$  plot (Fig. 4(c)), no discernible mass transport loss is observed in the high-current-density region; therefore, the semicircle associated with mass transport loss does not appear in the EIS spectrum. This seems to be due to the nanoscale thickness of the cathode (80 nm) as well as facile transport of extremely small  $\text{H}_2$  molecules through the AAO pores.<sup>14,18</sup> Interestingly, the anode activation resistance, which is usually known to be much smaller than the cathode activation resistance in symmetrically structured low-temperature SOFCs,<sup>9</sup> is clearly visible. We think that this is because the relatively thick (300 nm) Pt anode structure used to block the propagation of AAO pores to the electrolyte decreased the density of the triple phase boundary, where the electrode, electrolyte, and gas meet and electrochemical reactions preferentially occur, at the anode–electrolyte interface.<sup>21,32</sup>

Fig. 5(d), which shows the EIS spectra at a cell voltage of 0.6 V for all the samples, is presented for comparison. The activation resistance of the CZ sample is considerably larger than those of

the ZC and CZC samples, and that of the CZC sample is the smallest. Fig. 5(e) summarizes the ohmic, anodic activation, and cathodic activation resistances of the samples from the EIS measurement. On the basis of the previously reported ionic conductivity data of ALD YSZ ( $3.47 \times 10^{-5} \text{ S cm}^{-1}$  at  $450^\circ\text{C}$ )<sup>33</sup> and sputtered polycrystalline SDC ( $3 \times 10^{-3} \text{ S cm}^{-1}$  at  $450^\circ\text{C}$ ),<sup>22,34</sup> an area-specific resistance (ASR) of  $0.08 \Omega \text{ cm}^2$  can be obtained for the electrolytes in the ZC, CZC, and CZ samples, which is much smaller than the measured ohmic resistance ( $0.22 \pm 0.02 \Omega \text{ cm}^2$ ). The observed difference could be due to the sheet resistance of the porous Pt electrodes or the contact resistance between the microprobes and the electrodes.<sup>9,14</sup> The SDC layer may have been partially reduced and become more conductive near the anode side during operation in CZC and CZ samples,<sup>25</sup> which, however, will not significantly affect the size of the total ohmic resistance due to the much higher conductivity of SDC, *i.e.*, much smaller contribution to the ohmic resistance, than YSZ. The anodic activation resistance is about 50% lower in the CZC and CZ samples (0.10 and  $0.11 \Omega \text{ cm}^2$ , respectively) than in the ZC sample ( $0.22 \Omega \text{ cm}^2$ ) due to the presence of the catalytically active SDC–Pt interface.<sup>14,35,36</sup> Similarly, the cathodic activation resistances of the samples with the SDC–Pt cathodic interface (the ZC and CZC samples, 0.10 and  $0.17 \Omega \text{ cm}^2$ , respectively) are remarkably lower than that of the sample with the YSZ–Pt cathodic interface (the CZ sample,  $2.9 \Omega \text{ cm}^2$ ). The difference in the cathodic activation resistance between the two groups (12–30 times) is similar in magnitude to that in the exchange current density ( $j_0$ ) for oxygen surface exchange; *i.e.*, the  $j_0$  value for oxygen surface exchange of the YSZ–Pt interface is smaller than that of the doped ceria–Pt interface with an identical microstructure by 1–2 orders of

magnitude.<sup>14,35,36</sup> In summary, the CZC sample shows minimized activation loss at the cathode as well as at the anode.

More morphological details of the samples at the nanoscale are shown in Fig. 6, which summarizes cross-sectional STEM images and top-view FE-SEM images of the sputtered SDC and ALD YSZ surfaces of the samples, as well as high resolution TEM images. Several important observations that are closely relevant to the cell performance, *i.e.*, OCV, ohmic loss, and activation loss, can be made.

First, pinhole propagation in the Pt anode (Fig. 6(a)) or at grain boundaries (dark lines) in the SDC layer (Fig. 6(b) and (c)) is clearly blocked by the dense ALD YSZ layer without visible grain boundaries that covers the underlying rough surfaces in all the samples. In the CZ sample, for example, the surface of the sputtered SDC deposited directly on the Pt anode (Fig. 6(c-2)) initially has many surface defects, *e.g.*, pinholes (dark spots), which are largely covered by the ALD YSZ layer (Fig. 6(c-1)). The surface image of the ALD YSZ layer confirms the fine granular structure with grains  $\sim 10$  nm in size (Fig. 6(a-2), (b-2), and (c-1)). Conformal deposition of ALD YSZ on SDC grains is more clearly shown in Fig. 6(d) and (d-1): physical trench due to the surface grain-boundary between two SDC grains is completely filled with the dense ALD YSZ layer. Both SDC and YSZ layers are

also well-crystallized: the calculated lattice constants for SDC and YSZ are  $0.544 \pm 0.004$  nm and  $0.513 \pm 0.004$  nm, respectively. Considering the compositions of SDC (15.2 mol%) and YSZ (10.5 mol%) films deduced from the XPS analysis (Fig. 2), the measured lattice constants correspond well to the reported values for 15 mol% doped SDC ( $a = 0.544$  nm) and 10 mol% YSZ ( $a = 0.514$  nm) (Fig. 6(d-2) and (d-3)).<sup>6,22</sup> As a result, such a conformal and dense ALD YSZ layer seems to have helped achieve a high OCV of  $>1$  V even with the chemically unstable SDC electrolyte.

Second, the SDC layer is mostly composed of columnar grains of tens of nanometers in width in all the samples (Fig. 6(a)–(c)), which is a well-known characteristic of sputtered films.<sup>37</sup> Parallel alignment between the directions of the ionic conduction and the grain boundaries is beneficial for fast ionic conduction because the ionic transport is known to be facilitated along grain boundaries but significantly impeded across grain boundaries.<sup>6,38</sup> The ionic conductivity of ALD YSZ films with nanoscale grains is also known to be as high as that of single-crystalline YSZ.<sup>10</sup> This phenomenon stems from the overlapping of space charge layers near grain boundaries, which prevents grain-boundary potential buildup and expedites ionic transport across grain boundaries.<sup>39</sup> Overall, we speculate that

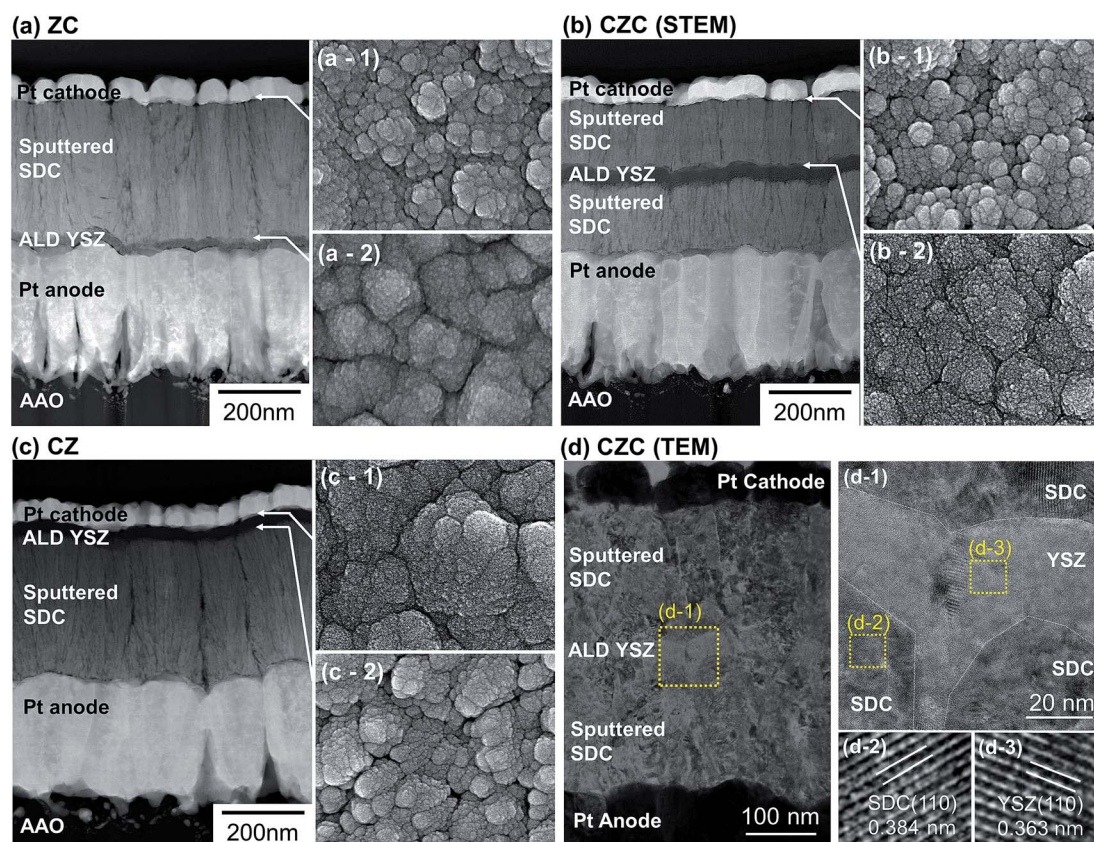


Fig. 6 (a–c) Cross-sectional STEM and top view FE-SEM images of the samples: (a) Cross-sectional STEM image, and top-view FE-SEM images of the (a-1) SDC surface and (a-2) YSZ surface of the ZC sample. (b) Cross-sectional STEM image and top-view FE-SEM images of the (b-1) SDC surface and (b-2) YSZ surface of the CZC sample. (c) Cross-sectional STEM image and top-view FE-SEM images of the (c-1) YSZ surface and (c-2) SDC surface of the CZ sample. Scale bars are identical for all images. (d) Cross-sectional TEM image of the CZC sample and (d-1) zoomed-in image of the yellow-dotted box in (d) (white-dotted lines represent the boundaries between SDC and YSZ). (d-2) and (d-3) are high-resolution TEM images of SDC and YSZ regions, which show the SDC (110) and YSZ (110) crystal planes, respectively.

the high ionic conductivity of the composite electrolyte has led to low ohmic loss in the cell operation.

Finally, it is notable that the surface of the SDC layer is also nanocrystalline, which yields a high surface grain-boundary density (Fig. 6(a-1) and (b-1)). The average surface grain size of the SDC layer on the cathode side in the CZC sample is  $19 \pm 4$  nm from AFM images (Fig. S3†). Surface grain boundaries are preferential sites for oxygen ion incorporation, possibly owing to the large population of oxide-ion vacancies.<sup>6,36</sup> Similarly, An *et al.* reported that the exchange current density at the nanocrystalline (average grain size of 38 nm) yttria-doped ceria (YDC) surface is several orders of magnitude higher than that at the sintered microcrystalline YDC surface in the temperature range of 350–450 °C.<sup>9</sup> Kim *et al.* also experimentally showed that the surface grain boundary in the YDC film is indeed the preferential location where oxide-ions incorporate at cathode side using high spatial resolution secondary ion mass spectrometry (nano-SIMS).<sup>40</sup> We speculate that the nanocrystalline SDC with fine grains and a high grain boundary density in our sample helped to improve the activation process and lower the activation loss in combination with the intrinsically high surface exchange rate of the SDC surface.

## Conclusion

The optimal design and the fabrication of a sandwich-structured sputtered SDC/ALD YSZ composite electrolyte for an AAO-supported TF-SOFC operating at low temperature (450 °C) was successfully demonstrated. By investigating the effect of the location of the extremely thin (25 nm) ALD YSZ layer, we found that the ALD YSZ layer embedded in the SDC electrolyte (360 nm) effectively blocks possible electrical/chemical shorts, enabling a high OCV while maintaining low ohmic and activation losses. To our knowledge, the power density of our SOFC (562 mW cm<sup>-2</sup> at 450 °C) is the highest among those of nanoporous substrate-supported thin film cells reported in this temperature range (450 °C and below). Considering the scalability of the AAO-supported architecture as well as the deposition techniques, *i.e.*, sputtering and ALD, we think the implications of this paper will open up a new possibility of low-temperature SOFCs for wider applications, including portable power sources, and commercialization.

## Conflicts of interest

There are no conflicts to declare.

## Acknowledgements

We acknowledge the financial support from the National Research Foundation under the Ministry of Education, Korea (NRF-2015R1D1A1A01058963) and by the Ministry of Trade, Industry and Energy (MOTIE), KOREA, through the Education Support program for Creative and Industrial Convergence (Grant Number N0000717). This research was also partially supported by Nano Material Technology Development Program

through the National Research Foundation of Korea (NRF) funded by the Ministry of Science, ICT and Future Planning (2009-0082580). We thank Kwonil Seong and Prof. Hyo-Suk Ahn for the assistance in AFM measurement.

## References

- 1 T. M. Gür, *Prog. Energy Combust. Sci.*, 2016, **54**, 1–64.
- 2 B. C. Steele and A. Heinzel, *Nature*, 2001, **414**, 345–352.
- 3 T. Mentoring, C. Michael and K. Head, *Science*, 2000, **19**, 702–740.
- 4 O. Yamamoto, *Electrochim. Acta*, 2000, **45**, 2423–2435.
- 5 J. Bae, S. Hong, B. Koo, J. An, F. B. Prinz and Y.-B. Kim, *J. Eur. Ceram. Soc.*, 2014, **34**, 3763–3768.
- 6 J. An, J. S. Park, A. L. Koh, H. B. Lee, H. J. Jung, J. Schoonman, R. Sinclair, T. M. Gür and F. B. Prinz, *Sci. Rep.*, 2013, **3**, 2680–2685.
- 7 W. Lee, H. J. Jung, M. H. Lee, Y.-B. Kim, J. S. Park, R. Sinclair and F. B. Prinz, *Adv. Funct. Mater.*, 2012, **22**, 965–971.
- 8 C.-C. Chao, C.-M. Hsu and F. B. Prinz, *ACS Nano*, 2011, **5**, 5692–5696.
- 9 J. An, Y.-B. Kim, J. Park, T. M. Gür and F. B. Prinz, *Nano Lett.*, 2013, **13**, 4551–4555.
- 10 J. H. Shim, C.-C. Chao, H. Huango and F. B. Prinz, *Chem. Mater.*, 2007, **19**, 3850–3854.
- 11 P.-C. Su, C.-C. Chao, J. H. Shim, R. Fasching and F. B. Prinz, *Nano Lett.*, 2008, **8**, 2289–2292.
- 12 J. D. Baek, Y.-J. Yoon, W. Lee and P.-C. Su, *Energy Environ. Sci.*, 2015, **8**, 3374–3380.
- 13 S. Ji, I. Chang, Y. H. Lee, J. Park, J. Y. Paek, M. H. Lee and S. W. Cha, *Nanoscale Res. Lett.*, 2013, **8**, 48–54.
- 14 S. Ji, G. Y. Cho, W. Yu, P.-C. Su, M. H. Lee and S. W. Cha, *ACS Appl. Mater. Interfaces*, 2015, **7**, 2998–3002.
- 15 S. Hong, Y. Lim, H. Yang, J. Bae and Y.-B. Kim, *J. Mater. Chem. A*, 2017, **5**, 2029–2036.
- 16 W. Yu, G. Y. Cho, S. Hong, W. Lee, Y. B. Kim, J. An and S. W. Cha, *Nanotechnology*, 2016, **27**, 415402.
- 17 S. Ji, Y. H. Lee, T. Park, G. Y. Cho, S. Noh, Y. Lee, M. Kim, S. Ha, J. An and S. W. Cha, *Thin Solid Films*, 2015, **591**, 250–254.
- 18 S. Hong, J. Bae, B. Koo and Y. B. Kim, *Electrochem. Commun.*, 2014, **47**, 1–4.
- 19 A. B. Stambouli and E. Traversa, *Renewable Sustainable Energy Rev.*, 2002, **6**, 433–455.
- 20 B. C. Steele, *Solid State Ionics*, 1995, **75**, 157–165.
- 21 R. O'Hayre, S. W. Cha, W. Colella and F. B. Prinz, *Fuel Cell Fundamentals*, Wiley, Hoboken, NJ, 2nd edn, 2008.
- 22 S. Zha, C. Xia and G. Meng, *J. Power Sources*, 2003, **115**, 44–48.
- 23 H. Inaba and H. Tagawa, *Solid State Ionics*, 1996, **83**, 1–16.
- 24 I. Chang, J. Bae, J. Park, S. Lee, M. Ban, T. Park, Y. H. Lee, H. H. Song, Y.-B. Kim and S. W. Cha, *Energy*, 2016, **104**, 107–113.
- 25 C.-W. Kwon, J.-W. Son, J.-H. Lee, H.-M. Kim, H.-W. Lee and K.-B. Kim, *Adv. Funct. Mater.*, 2011, **21**, 1154–1159.
- 26 H.-S. Noh, J. Hong, H. Kim, K. J. Yoon, J.-H. Lee, B.-K. Kim and J.-W. Son, *J. Ceram. Soc. Jpn.*, 2015, **123**, 263–267.

- 27 R. Leah, A. Bone, E. Hammer, A. Selcuk, M. Rahman, A. Clare, S. Mukerjee and M. Selby, *ECS Trans.*, 2017, **78**, 87–95.
- 28 M. D. Groner, J. W. Elam, F. H. Fabreguette and S. M. George, *Thin Solid Films*, 2002, **413**, 186–197.
- 29 T. H. Kwon, T. Lee and H. I. Yoo, *Solid State Ionics*, 2011, **195**, 25–35.
- 30 K. Eguchi, T. Setoguchi, T. Inoue and H. Arai, *Solid State Ionics*, 1992, **52**, 165–172.
- 31 A. Leonide, Y. Apel and E. Ivers-Tiffée, *ECS Trans.*, 2009, **19**, 81–109.
- 32 J. Park, Y. Lee, I. Chang, W. Lee and S. W. Cha, *Thin Solid Films*, 2015, **584**, 125–129.
- 33 J. H. Shim, S. Kang, S. W. Cha, W. Lee, Y.-B. Kim, J. S. Park, T. M. Gür, F. B. Prinz, C.-C. Chao and J. An, *J. Mater. Chem. A*, 2013, **1**, 12695–12705.
- 34 Y. Yoo, *J. Power Sources*, 2006, **160**, 202–206.
- 35 Z. Fan and F. B. Prinz, *Nano Lett.*, 2011, **11**, 2202–2205.
- 36 J. H. Shim, J. S. Park, T. P. Holme, K. Crabb, W. Lee, Y.-B. Kim, X. Tian, T. M. Gür and F. B. Prinz, *Acta Mater.*, 2012, **60**, 1–7.
- 37 S. Hong, D. Lee, Y. Lim, J. Bae and Y.-B. Kim, *Ceram. Int.*, 2016, **42**, 16703–16709.
- 38 J. S. Park, Y.-B. Kim, J. An and F. B. Prinz, *Solid State Commun.*, 2012, **152**, 2169–2171.
- 39 J. An, J. Bae, S. Hong, B. Koo, Y.-B. Kim, T. M. Gür and F. B. Prinz, *Scr. Mater.*, 2015, **104**, 45–48.
- 40 Y. B. Kim, J. S. Park, T. M. Gür and F. B. Prinz, *J. Power Sources*, 2011, **196**, 10550–10555.